



## An Acoustofluidic Trap and Transfer Approach for Organizing a High Density Single Cell Array

Journal:	<i>Lab on a Chip</i>
Manuscript ID	LC-ART-02-2018-000196.R1
Article Type:	Paper
Date Submitted by the Author:	09-Jun-2018
Complete List of Authors:	<p>Ohiri, Korine; NSF Research Triangle Materials Research Science and Engineering Center; Duke University, Department of Mechanical Engineering and Materials Science</p> <p>Kelly, Sean; Duke University, Department of Mechanical Engineering and Materials Science</p> <p>Motschman, Jeffrey; Duke University, Department of Mechanical Engineering and Materials Science</p> <p>Lin, Kevin; Duke University Department of Pharmacology and Cancer Biology</p> <p>Wood, Kris; Duke University Department of Pharmacology and Cancer Biology</p> <p>Yellen, Benjamin; Duke University, Department of Mechanical Engineering and Materials Science; NSF Research Triangle Materials Research Science and Engineering Center; Duke University Department of Biomedical Engineering</p>

# An Acoustofluidic Trap and Transfer Approach for Organizing a High Density Single Cell Array

Korine A. Ohiri,<sup>1,2</sup> Sean T. Kelly,<sup>1</sup> Jeffrey D. Motschman,<sup>1</sup> Kevin H. Lin,<sup>3</sup> Kris C. Wood,<sup>3</sup> Benjamin B. Yellen<sup>1,2,4,\*</sup>

1. Department of Mechanical Engineering and Materials Science, Duke University, Durham, NC 27708, USA

2. NSF Research Triangle Materials Research Science and Engineering Center, Duke University, Durham, NC 27708, USA

3. Department of Pharmacology and Cancer Biology, Duke University, Durham, NC 27708, USA

4. Department of Biomedical Engineering, Duke University, Durham, NC 27708, USA

**\*Corresponding Author:** *E-mail:* yellen@duke.edu

**Submitted to:** *Lab on a Chip*

**Key terms:** single cell isolation, high throughput, bulk acoustic waves, lab-on-a-chip, microfluidics, acoustofluidics

## Abstract

We demonstrate a hybrid microfluidic system that combines fluidic trapping and acoustic switching to organize an array of single cells at high density. The fluidic trapping step is achieved by balancing the hydrodynamic resistances of three parallel channel segments forming a microfluidic trifurcation, the purpose of which was to capture single cells in a high-density array. Next, the cells were transferred into adjacent larger compartments by generating an array of streaming micro-vortices to move the cells to the desired streamlines in a massively parallel format. This approach can compartmentalize single cells with efficiencies of  $\approx 67\%$ , in compartments that have diameters on the order of  $\sim 100$   $\mu\text{m}$ , which is an appropriate size for single cell proliferation studies, and other single cell biochemical measurements.

## 32 **Introduction**

33           Single cell analysis is enabling new insights into the heterogeneity within a cell  
34 population that were previously concealed using traditional bulk ensemble measurement  
35 techniques.<sup>1-3</sup> The field is currently receiving significant attention<sup>4-7</sup> and is expected to open up a  
36 plethora of applications in basic and clinical research for fields ranging from oncology, to  
37 immunology, neuroscience, and beyond.<sup>8-12</sup> Accordingly, there has been great interest in  
38 innovating new techniques that can organize single cells into discrete chambers and monitor their  
39 response to various stimuli, such as the presence of a drug, growth factor, or another cell.

40           One of the earliest single cell organization approaches is fluorescent activated cell sorting  
41 (FACS) which to this day is still being used to deposit single cells into each well of a 96-well or  
42 384-well plate.<sup>13</sup> However, this plate-based format severely limits the number of cells that can be  
43 analyzed in parallel. Additionally, the large volumes used in plate-based FACS sorting is poorly  
44 suited for growing single cells in isolation and many types of single cell measurements, such as  
45 the analysis of secreted cytokines, and cell-cell communication. Due to their smaller volumes,  
46 microfabricated single cell analysis platforms are better suited to these types of measurements<sup>6, 7,</sup>  
47 <sup>14</sup>, and have the additional advantage of increasing the imaging speed and reducing the  
48 consumption of expensive reagents.

49           Single cell arrays have been organized with passive cell capture mechanisms, such as  
50 sedimentation into micro-wells or fluidic trapping in weirs,<sup>15-22</sup> and active capture mechanisms  
51 based on the use of magnetic, electric, or acoustic field to transport cells to desired locations.<sup>23-26</sup>  
52 Passive separation mechanisms are usually high throughput and have the advantage of reduced  
53 complexity; however, these approaches have various limitations, such as low single cell  
54 organization efficiency in the case of stochastic sedimentation approaches<sup>27-29</sup> or high fluidic  
55 shear of progeny in the case of hydrodynamically trapped cells,<sup>21</sup> and both are generally  
56 incapable of organizing more than one type of single cell into an array. Variations on these  
57 approaches have shown the ability to transfer the trapped cells to larger chambers, such as by  
58 inverting a microfluidic device<sup>30, 31</sup> or by exploiting the deformability of cells to squeeze them  
59 into an adjacent compartment.<sup>32</sup> However, it can be a challenge to automate the passive  
60 sedimentation process and exchange fluids, such as fresh media and drugs, without disturbing the  
61 assembled cell pattern. Additionally, cell damage can occur during cell deformation-based  
62 trapping approaches, which can reduce the viability of the transferred cells.

63           Alternatively, active field-based manipulation approaches are more programmable and  
64 can control the positions of single cells with micron precision; however, they require multi-layer  
65 devices and external power sources, which both increases complexity and suffers from other  
66 fundamental limitations. For example, magnetic circuit approaches have the advantage of easy  
67 scaling to control many thousands of single cells in parallel; however, magnetic systems require  
68 magnetic nanoparticles to label the cells and manipulate them by a magnetic force.<sup>33, 34</sup>  
69 Dielectrophoretic approaches have the potential for label-free cell manipulation by utilizing the  
70 dielectric contrast of cells relative to the surrounding media; however, this technique is not  
71 amenable to high ionic strength fluids, such as cell culture media, and necessitates the use of  
72 isotonic buffers to allow the electric fields to penetrate the fluid. Recently developed  
73 optoelectronic approaches have similar problems as dielectrophoretic systems,<sup>35, 36</sup> though some  
74 of these limitations have recently been surmounted with the development of phototransistors that  
75 can operate directly in cell culture media.<sup>37, 38</sup>

76           Acoustic approaches have demonstrated the ability to control the positions and  
77 orientations of single cells in a label-free manner, and they can additionally be operated directly  
78 in cell culture media. Importantly, these approaches have been previously shown to hold multiple  
79 cells individually<sup>39</sup> and cluster groups of cells in microwells.<sup>40</sup> “Bulk acoustic wave” (BAW)  
80 devices can be built from single layer silicon or glass microfluidic channels and designed to  
81 resonate at well-characterized frequencies that correspond to the device geometry.<sup>41-45</sup> Moreover,  
82 these systems can be operated with a simple piezoelectric transducer mounted underneath the  
83 device; however, BAW devices have limited ability to change the position of the focusing nodes,  
84 and thus have mainly been used in bulk continuous flow sorting applications. Surface acoustic  
85 wave (SAW) devices can overcome some of these limitations by allowing the pressure nodes to  
86 be controlled independently of the microfluidic channel geometry.<sup>46-49</sup>

87           Thus, given the constraints above, it is reasonable to assert that a combination of both  
88 passive and active methods should offer the most adaptable, gentle, and parallelizable approach  
89 to organize a single cell array. Towards this end, we have developed a “trap and transfer”  
90 process, which exploits the synergistic combination of passive hydrodynamic trapping to  
91 establish the initial positions of the single cells in an array, and then an active acoustic transfer  
92 step to move the cells to larger chambers that are more suitable for single cell measurements.  
93 After considering the different acoustic transfer approaches, we ultimately decided to use a BAW

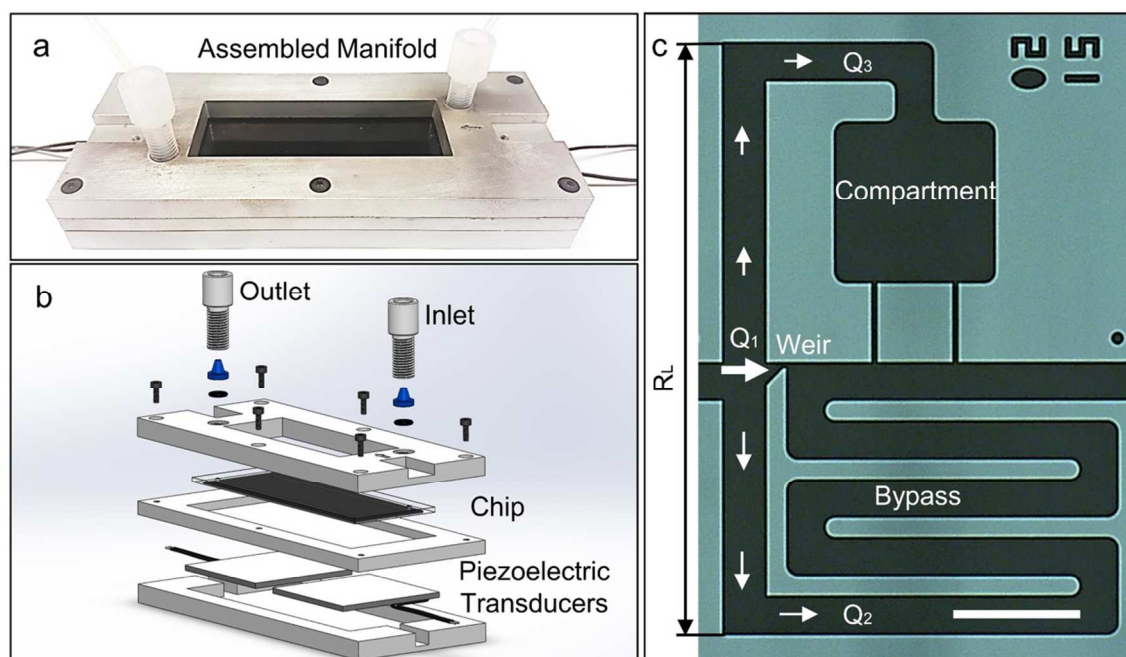
94 transfer mechanism because of its simplicity, biocompatibility, and because the microfluidic and  
95 acoustic functionality can be seamlessly integrated into a single device layer. Uniquely, our  
96 hybrid BAW transfer process demonstrates for the first time the parallel, high-precision  
97 manipulation of individual cells with an array of acoustically induced streaming vortices. With  
98 this approach, we have generated an array of single cells in low-shear compartments with an  
99 efficiency of  $\approx 67\%$ .

100

## 101 Results and Discussion

102 The basic setup is shown in Figure 1(a-b), presenting one of several different chip  
103 designs. This chip has dimensions consistent with a glass slide (i.e. 25 x 75 mm) and fits 3,840  
104 individual compartments. This design consists of 96 parallel microfluidic channels, each having  
105 40 compartments in series at an areal density of approximately 4 compartments per  $\text{mm}^2$   
106 ( $\text{cmpts}/\text{mm}^2$ ). We have also tested smaller devices with the same basic design that have a  
107 footprint of 15 mm x 25 mm consisting of 16 parallel channels with 31 compartments in series  
108 with a total of 496 compartments. To demonstrate the feasibility of higher density designs, we  
109 also tested chips that have a density of  $\approx 12 \text{ cmpts}/\text{mm}^2$ , allowing for more than 5,000 cells to be  
110 organized in a device the size of a glass slide (see Electronic Supplementary Information for  
111 Alternative Microfluidic Designs).

112



113

114 **Figure 1.** Acoustofluidic single cell array. (a) Image of chip in the aluminum manifold. (b)  
 115 Schematic of entire set-up indicating the location of the chip, inlet, outlet, and piezoelectric  
 116 transducers. Here, the piezoelectric transducers were acoustically coupled to the microfluidic  
 117 chip using electrode gel (see Materials and Methods for more details).” (c) Image of individual  
 118 acoustofluidic element with characteristic length ( $R_L$ ) and comprised of a weir (1), bypass (2),  
 119 and compartment region (3). Scale bar indicates 100  $\mu\text{m}$ .

120  
 121 The basic switching junction is a trifurcation, consisting of the weir (i.e. primary trap site), a  
 122 bypass channel, and a cellular compartment (Figure 1(c)). The hydrodynamic flow profile was  
 123 finely tuned to reliably capture single cells at the weirs, without unintentionally transferring the  
 124 cells into the compartments, except when desired.

125

### 126 *Design of Hydrodynamic Circuit*

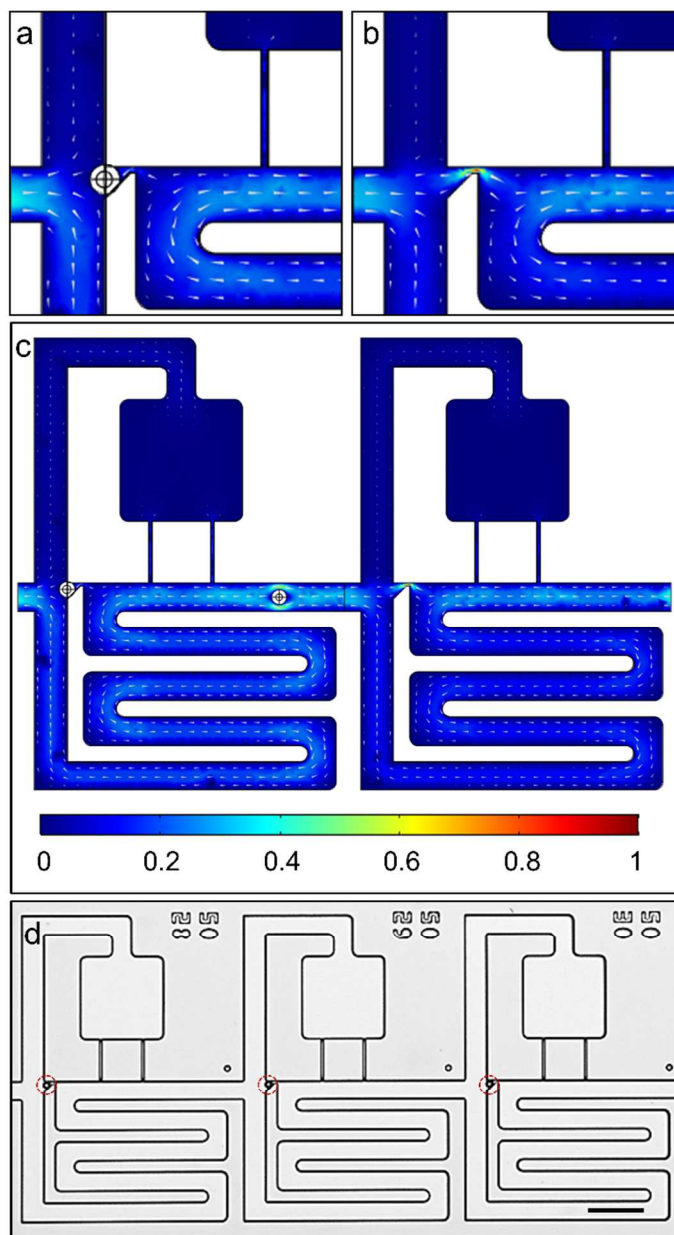
127 We optimized the hydrodynamic trapping step by tuning the three volumetric flow rates  
 128 ( $Q_1$ ,  $Q_2$ , and  $Q_3$ ), in which the hydrodynamic resistance of each branch is carefully controlled.  
 129 The overall pressure drop across the trifurcation allows the fluidic path to be modeled as three  
 130 parallel resistive paths, with each segment approximated by the well-known approximation for  
 131 hydrodynamic resistance in a rectangular channel:<sup>50</sup>

$$132 \quad R_{rec} \approx \frac{12\eta L}{(wh^3) - 0.63h^4}, w > h \quad (1)$$

133 where  $\eta$  is the dynamic viscosity of the fluid,  $L$  is the length of the channel, and where  $w$  and  $h$   
 134 represent the cross-sectional dimensions of the channel, in which the smaller of the two  
 135 dimensions is defined as  $h$ . The geometry of the weirs is designed such that an unoccupied weir  
 136 has the lowest fluidic resistance, whereas an occupied weir has higher fluidic resistance than the  
 137 bypass channel. This design ensures that after a weir traps a single cell, subsequent cells are  
 138 diverted towards the bypass channel until one of them gets trapped in the next unoccupied weir.  
 139 This process allows the weirs across the entire chip to be loaded within minutes.

140 Since our device was fabricated through single-level Silicon etch, we tuned the fluid  
 141 resistances by adjusting the lengths and widths of each channel section. The bypass channel was  
 142 designed to have a width commensurate to several cell diameters (in our case 35  $\mu\text{m}$ ), which  
 143 helped to reduce clogging but required long serpentine bypass channels to match the desired  
 144 resistance ratios. The weirs have widths of 6  $\mu\text{m}$  and lengths of 4  $\mu\text{m}$ , from which we derive a

145 condition that the length of the bypass channel must be at least  $\sim 1$  mm long to maintain the  
146 condition  $R_2/R_1 > 2$ , which ensures that most fluid flow goes through the trap as compared to the  
147 bypass segment, thus increasing the probability of capturing cells in the weirs. To avoid  
148 unintentionally moving cells into the compartments prematurely, we included physical  
149 constrictions in the compartment region to raise the fluidic resistance. This section was designed  
150 to achieve a resistance ratio  $R_3/R_2 > 2$  with a similar purpose of biasing most fluid flow to go  
151 through the bypass segment compared to the compartment. To visualize the flow patterns, we  
152 show COMSOL calculations of the normalized velocity for the case when the weir is occupied  
153 (Figure 2(a)) or is empty (Figure 2(b)). As expected, the flow velocity is highest through the  
154 unoccupied weir, followed by the bypass region, and finally lowest through the compartment  
155 region and occupied weir (Figure 2(c)).



156

157 **Figure 2.** Demonstration of hydrodynamic trapping in trifurcation design. COMSOL simulation  
 158 of an (a) occluded weir, (b) unoccupied weir, and (c) the entire acoustofluidic element. (d) Beads  
 159 captured in trap sites of acoustofluidic array. Legend indicates normalized velocity and scale bar  
 160 represents 100  $\mu\text{m}$ .

161

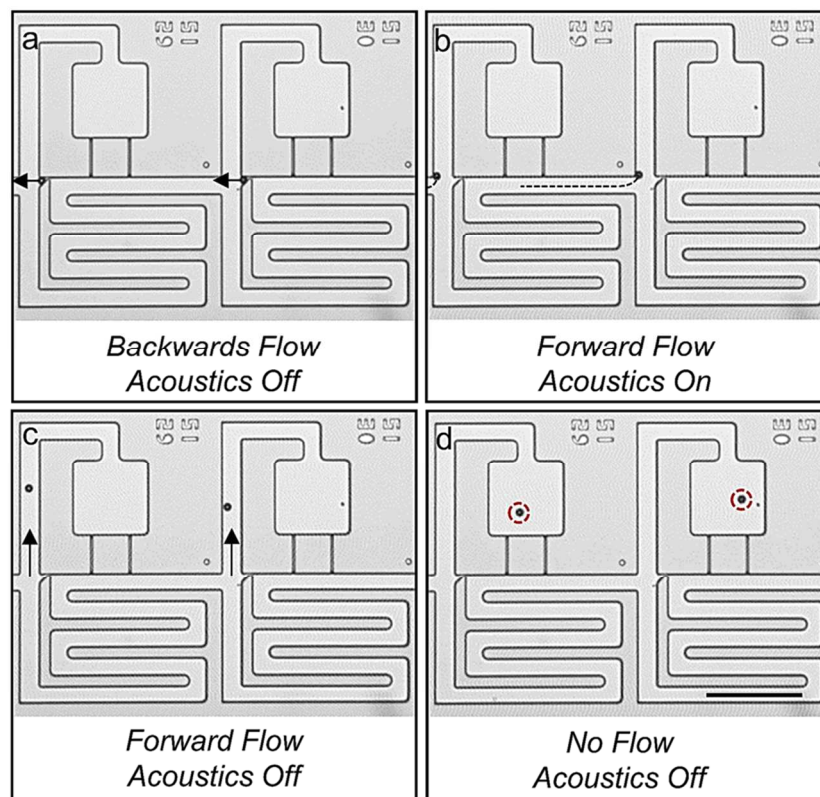
162 Based on these simulations for the velocity field, we calculated the volumetric flow rate by  
 163 averaging the velocity across planes entering the trap, bypass, and compartment region then  
 164 multiplying by the corresponding cross-sectional area. In this way, we obtained values of  $Q_1/Q_2$

165  $\approx 2.4$  and  $Q2/Q3 \approx 3.6$ , which is consistent with our analytical predictions. To confirm these  
166 predictions, we injected  $15\ \mu\text{m}$  polystyrene beads ( $50,000$  beads/mL; Sigma Aldrich Corp.) into  
167 the device and flowed them through the chip at a flow rate of  $50\ \mu\text{L}/\text{min}$ . We used large beads  
168 for the purpose of completely occluding the weir, which causes the flow profile through the  
169 region to more closely match the expected behavior of deformable cells entering the trap. As  
170 expected, beads first populate the weir, thus decreasing flow through this region and causing  
171 subsequent beads to travel through the bypass (Figure 2(d), see Supplementary Movie 1). In this  
172 way, cells and beads can be hydrodynamically loaded into weirs, then intentionally transferred  
173 into the compartment region when an acoustic force is activated.

174

#### 175 *Optimization of Acoustic Transfer Step*

176 After hydrodynamic trapping (Figure. 3(a)), the beads or cells can be transferred into the  
177 compartment regions by reversing the fluid flow to release them from their weirs and then  
178 establishing a slow forward flow to move them into the adjacent compartments under acoustic  
179 excitation. As can be seen, acoustic excitation of the chip caused the beads to be strongly  
180 attracted to the leading corner of the compartment region, which is defined here as the transfer  
181 point depicted as the end point of the dashed line trajectory in Figure 3(b). Thereafter, the  
182 acoustic transducer was turned off and forward pressure was used to push the beads into the low-  
183 shear compartment regions (Figure 3(c), see Electronic Supplementary Information for Shear  
184 Stress Through the Acoustofluidic Element) to the final loading sites (Figure 3(d), see  
185 Supplementary Movie 2). Thus, the purpose of the acoustic switch is to move the beads into the  
186 streamlines that pass through the compartment. It is important to note that during this acoustic  
187 switching step, we kept the flow at a low speed (e.g.  $< 50\ \mu\text{m}/\text{s}$ ) to allow the acoustic force to  
188 dominate fluid convection.



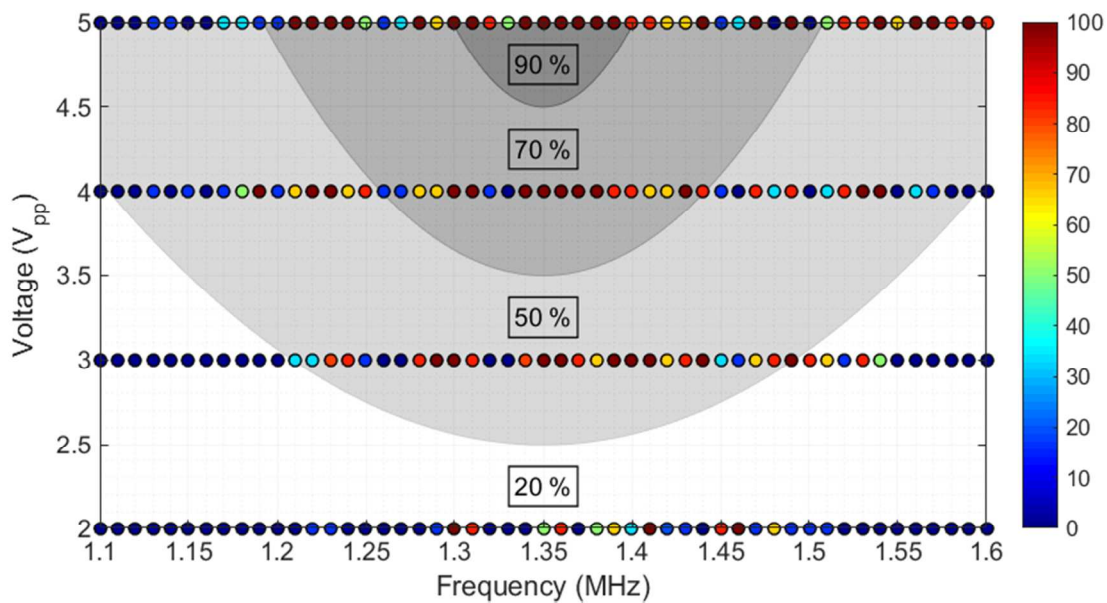
189

190 **Figure 3.** Image sequence detailing the acoustic switching mechanism. (a) Beads are captured in  
 191 weirs using an oscillatory pressure profile. Once each site is occupied, beads are unloaded from  
 192 weirs using backward flow. (b) Beads are slowly propelled towards the trifurcation junction  
 193 (their paths are indicated by the dotted lines) using positive pressure and are acoustically trapped  
 194 at the leading corner of the compartment region. (c) Beads are flowed into the compartment  
 195 region. (d) Beads are loaded in the compartment region. Scale bar indicates 200  $\mu\text{m}$ .

196

197 To find the optimal parameters for acoustic attraction to the corners, we injected 8.5  $\mu\text{m}$   
 198 polystyrene beads (50,000 beads/mL; Sigma Aldrich Corp.) into the chip and tracked the bead  
 199 motion towards the corner at frequencies ranging from 1.1 to 1.6 MHz and applied voltages  
 200 ranging from 2 to 5  $V_{pp}$  (as read by the oscilloscope following amplification). This frequency  
 201 range coincides with the expected structural resonance of the microfluidic channel ( $R_L$ , Figure  
 202 1), which was 555  $\mu\text{m}$  long and is matched to an acoustic wavelength of 1.35 MHz. Our method  
 203 involved first applying backward pressure to remove the beads from the weirs and away from the  
 204 switching junction, and next applying slow forward pressure to move towards the switching  
 205 junction when the acoustic field was turned on. A successful switching event is one in which the

206 bead was captured by the corner within 5 seconds. We used a 10X objective to visualize many  
207 switching processes simultaneously in a large field of view, which allowed us to obtain at least 6  
208 measurements for each voltage/frequency pair, and the results are provided in Figure 4. As a  
209 visual aid, the data points are color-coded, in which red depicts 100% capture on the corner and  
210 blue depicts 0% capture. As a guide to the eye, we also provide a contour plot to show the  
211 conditions where trapping was most efficient, which was in the range of 1.35 – 1.42 MHz and at  
212 higher voltages.



213

214 **Figure 4.** Color plot of switching efficiencies of polystyrene beads onto the leading corners of  
215 the compartment region upon acoustic excitation ( $n=6$  compartments). Shaded regions indicate  
216 average switching efficiencies over the specified range.

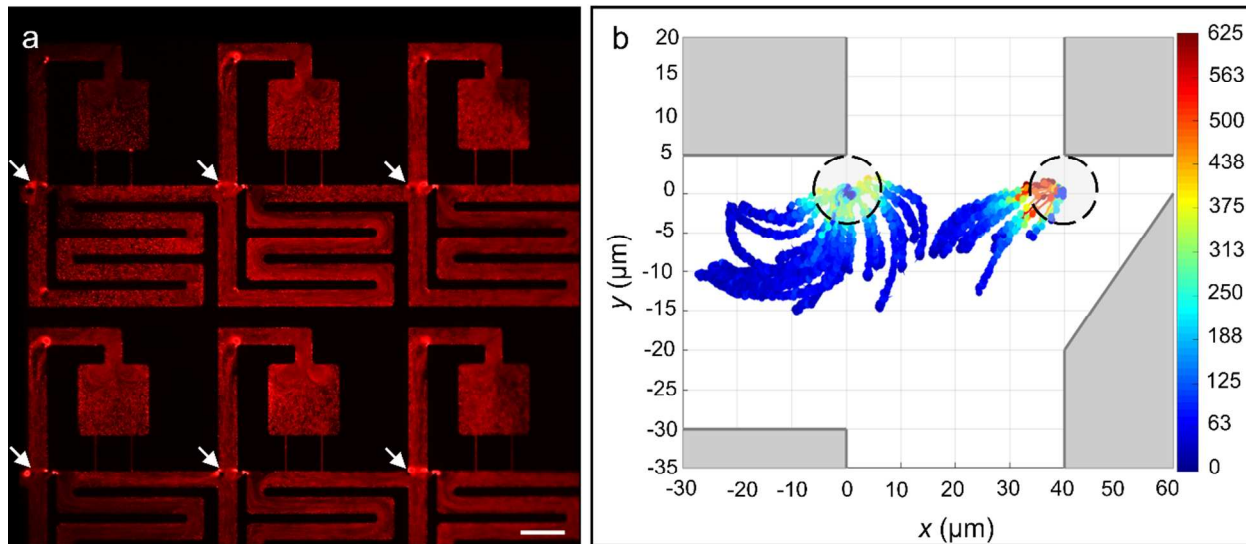
217

218 To confirm that this optimal frequency was caused by the channel dimensions and not by  
219 a characteristic resonance of the PZT actuator, we additionally tested this effect with PZT  
220 transducers having different resonant frequencies (705 kHz, 1.35 MHz, 2.9 MHz). In all cases,  
221 the devices showed peak performance around 1.40 MHz, similar to the results shown in Figure 4.  
222 It is clear from Figure 4 that the particle switching effect has strong frequency dependence,  
223 which would imply that the acoustic fields are amplified due to certain structural features of the  
224 microfluidic channel; however, these measurements alone were not sufficient to conclude  
225 whether the effect was due to the acoustic radiation force in a standing acoustic wave or whether

226 the particles are following the flow patterns produced by streaming vortices near the sharp  
227 corner.

228 To better understand the acoustically excited flow patterns, we next injected 200 nm red  
229 fluorescent tracer particles (0.1 wt % in CTAB; Sigma Aldrich Corp) into the fluid and used long  
230 exposures to enable visualization of the streaming patterns near the trifurcation. In the absence of  
231 an acoustic field, the flow patterns are random as expected (see Supplementary Movie 3). When  
232 the transducer was actuated at 1.4 MHz and 5 V<sub>pp</sub>, we observed very clear streaming vortices,  
233 which spanned the length of the channels and were present with minor variations across all the  
234 junctions in each field of view (Figure 5(a)). The high consistency of the streaming vortices  
235 across the entire chip indicated that it is caused by the specific structural features of the  
236 compartment rather than the specific position of the PZT transducer, overall size of the chip, or  
237 other macroscale features. Streaming vortices form at all the sharp corners in the microfluidic  
238 channels and establish steady state circulatory flow, which rotates in different directions  
239 depending on the excitation frequency. Micron-sized objects are attracted to the center of these  
240 vortices and rotate continuously inside them. Since the acoustic transducer is excited only when  
241 the forward flow is established, the beads or cells are captured at the first vortex that they  
242 experience, which is usually the leading corner as specified in Figure 5(a). From there, these  
243 objects are carried along the laminar flow paths that terminate inside the compartments when the  
244 acoustic transducer is turned off and forward flow is applied. We note here that while only  
245 streaming vortices present at the trifurcation point are used for our transfer mechanism, multiple  
246 vortices form throughout the device, particularly at locations with sharp edges and low flow (e.g.  
247 entrance corner to the compartment region, upper bend in the compartment region, throat of the  
248 compartment region).

249

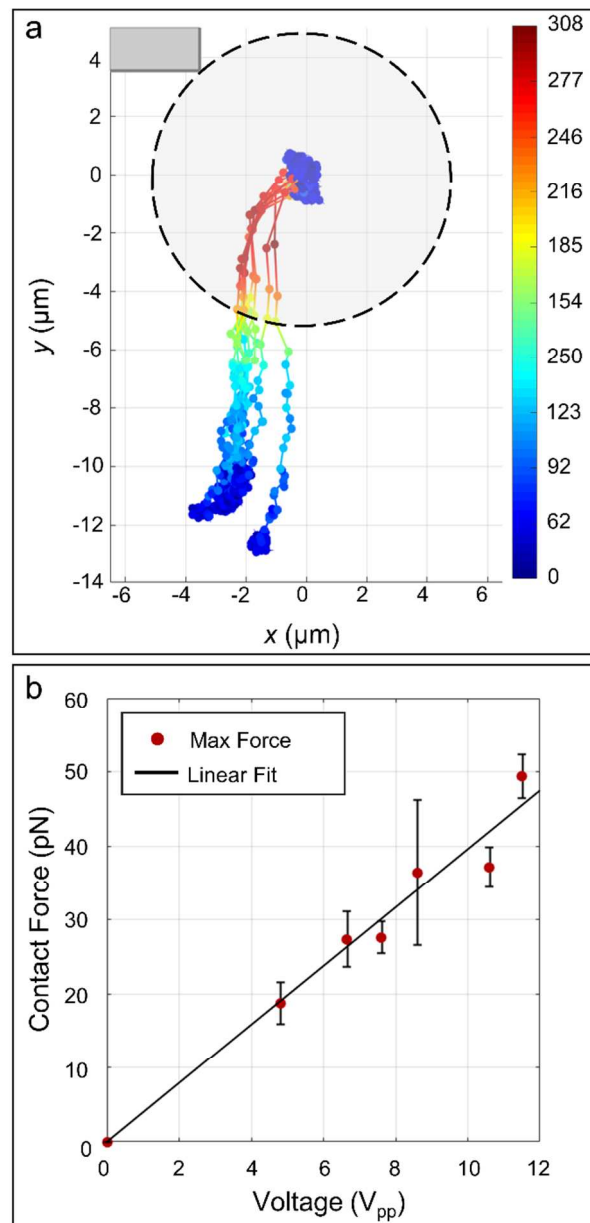


250  
251 **Figure 5.** (a) Red fluorescent image of nanoparticles under acoustic excitation at 1.4 MHz and 5  
252  $V_{pp}$ . (b) Normalized velocity magnitudes of 8.5  $\mu\text{m}$  polystyrene beads approaching the entrance  
253 corner of the compartment region. Here, the dashed circles indicate the outline of the bead (or  
254 cell) at its final position. Scale bar indicates 100  $\mu\text{m}$ .

255 Further evidence that the transfer effect is due to the presence of streaming vortices was  
256 obtained by tracking the trajectories of individual beads in the vicinity of each corner. Using the  
257 same 8.5  $\mu\text{m}$  beads described above, we tracked the trajectories of  $\approx 44$  individual particles upon  
258 acoustic excitation at 1.4 MHz and 5  $V_{pp}$  and overlaid them on the same plot (Figure 5(b)). As a  
259 visual aid, the data points are colored according to their instantaneous velocity. The overall  
260 shapes of the trajectories, their good match with the shapes of the streaming vortices, as well as  
261 the strong spatial dependence of the bead velocity, all provide strong evidence that acoustic  
262 confinement at the entrance corner of the compartment region is due to acoustic streaming. This  
263 finding is consistent with previous studies in which large particles and cells were trapped in  
264 steady acoustic streaming patterns around oscillating edges.<sup>51-54</sup>

265 Following this, to better characterize the strength and driving mechanism of the acoustic  
266 switching effect, we also measured the peak velocity of the beads as a function of the applied  
267 voltage. These measurements were taken with a high-speed camera at 240 frames per second,  
268 which could quantify trajectories of up to  $\sim 1$  mm/s. The highest velocities were recorded close  
269 to the sharp corner, which allowed us to approximately measure the contact force based on  
270 extrapolation from the fluid drag on a sphere Figure 6(a). The results indicate that the peak

271 contact force is linearly related to the magnitude of the applied voltage, similar to the linear  
272 relationships observed by others at high acoustic excitations.<sup>55</sup> We estimate that at the strongest  
273 acoustic excitations, the contact force is less than 100 pN, and should thus be gentle on the cells.  
274 As can be seen, however, this contact force is sufficient to hold the particles in place at the  
275 entrance corner to the compartment region during our transfer process. From Figure 6(b), it is  
276 clear that the peak contact force scales linearly with voltage, which contrasts with the acoustic  
277 radiation force that should roughly scale quadratically with the excitation voltage.<sup>41</sup> Further, as a  
278 final piece of evidence, we note that both highly elastic PDMS-based microparticles and stiff  
279 polystyrene beads are attracted to the same position with comparable velocities. Since it is well  
280 known that PDMS particles suspended in aqueous fluids exhibit an effective negative acoustic  
281 contrast factor, whereas polystyrene beads exhibit a positive acoustic contrast, these two  
282 materials should not be attracted to the same points in an acoustic energy landscape (see  
283 Electronic Supplementary Information for Material Dependence of Acoustic Radiation Force).  
284 The combination of these measurements thus allows us to reasonably conclude that the acoustic  
285 switching mechanism is based on acoustic streaming rather than an acoustic radiation force.<sup>41</sup>



286

287 **Figure 6.** (a) Trajectories of 8.5 μm polystyrene beads approaching the entrance corner of the  
288 compartment region. (b) Plot of maximum force before contact versus voltage.  $R^2 = 0.9656$ .

289

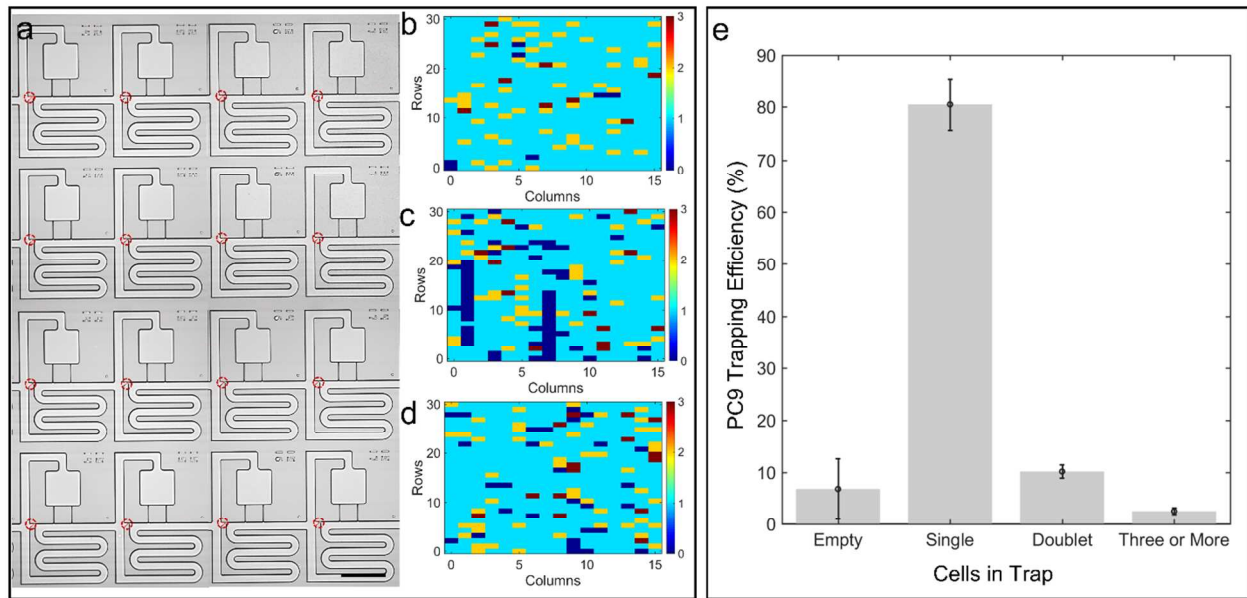
### 290 *Generation of Single Cell Arrays*

291 After optimizing the acoustic transfer step, we next sought to demonstrate the feasibility  
292 of this trap and transfer approach to organize a single cell array in a highly parallel manner.

293 Towards this end, we first quantified the ability to fluidically trap PC9 cancer cells (400,000

294 cells/mL) in the weirs and demonstrated the consistent ability to achieve a weir occupancy  
 295 efficiency of  $80 \pm 5\%$  single cells (Figure 7(a-e)). Blue, cyan, yellow, and red indicate 0, 1, 2,  
 296 and 3 trapped cells, respectively. We expect that the efficiency can be improved by reducing the  
 297 number of cell doublets entering the chip, and limiting cellular debris, which leads to clogging of  
 298 some of the channel (two blockages are clearly shown in Figure 7(c), and doublets are colored in  
 299 yellow).

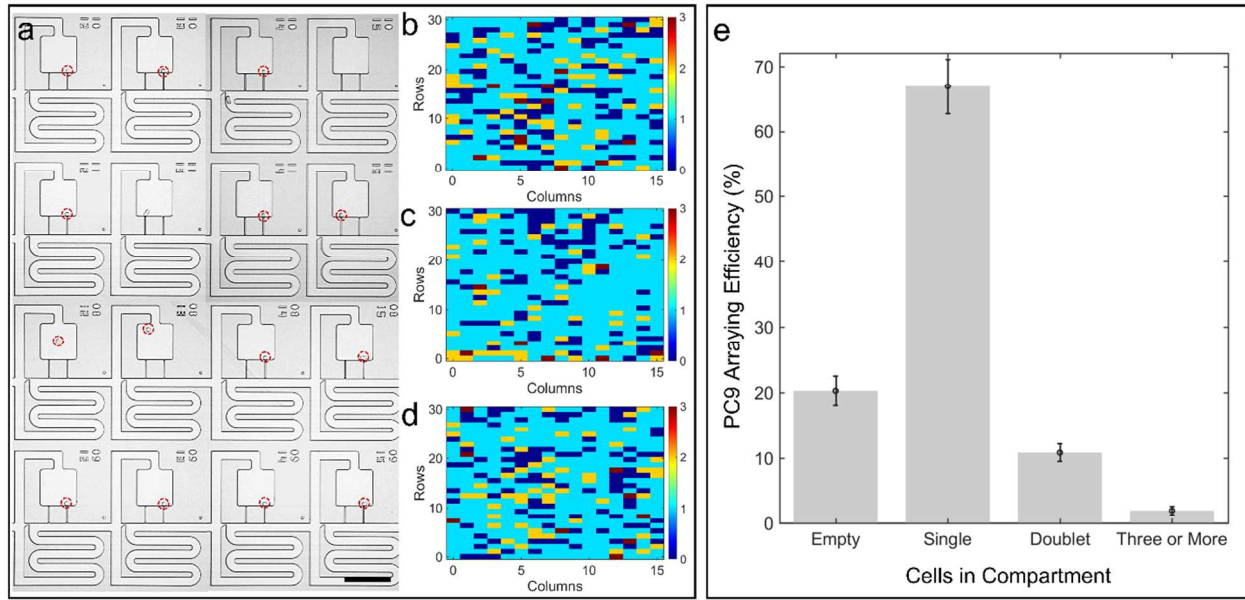
300



301

302 **Figure 7.** Trapping efficiency for PC9 cells in the weirs of the trifurcation. (a) Representative  
 303 image of trapped cells. Number of cells captured in individual trap sites for trial (b) one, (c) two,  
 304 and (d) three. (e) Distribution of cells in  $n = 3$  acoustofluidic chips. Scale bar indicates  $200\ \mu\text{m}$ .

305 Next, we transferred the cells into their corresponding adjacent compartments using an acoustic  
 306 sweep from 1.35 to 1.42 MHz, with a sweep rate of 1 Hz for over one second at an excitation of  
 307  $16\ \text{V}_{\text{pp}}$  (Figure 8(a), see Supplementary Movie 4). As can be seen, after the second step of this  
 308 process, we were able to consistently obtain a single cell array with an efficiency of  $67 \pm 4\%$   
 309 (Figure 8(b-e)).



310  
 311 **Figure 8.** Arraying efficiency for PC9 cells in the compartment region of the trifurcation. (a)  
 312 Representative image of arrayed cells. Number of cells captured in individual array sites for trial  
 313 (b) one, (c) two, and (d) three. (e) Distribution of cells in  $n = 3$  acoustofluidic chips. Scale bar  
 314 indicates 200  $\mu\text{m}$ .

315 This number represents the fraction of single cells present in the compartment regions of the  
 316 acoustofluidic chip, and is dependent on the number of single cells originally trapped in the weirs  
 317 prior to acoustic switching. Accordingly, this data indicates that the acoustic switching efficiency  
 318 is approximately 83 %.

319

## 320 Conclusion

321 In conclusion, we have demonstrated a trap and transfer process for organizing a high-  
 322 density array of single cells. This approach relies on a combination of hydrodynamic capture of  
 323 cells in weirs and then transfer of the cells into more spacious compartment chambers using an  
 324 array of acoustic streaming vortices as local switches. To our knowledge, this is the first  
 325 demonstration of the consistent generation of an array of streaming vortices for use in massively  
 326 parallel acoustic control of single cells. We used this approach to generate a single cell array  
 327 with an arraying efficiency of  $\approx 67\%$ , allowing us to array thousands of cells on a glass slide  
 328 sized device. These efficiencies may be improved by functionalizing the microfluidic channels  
 329 with a non-fouling brush and by refining our protocols to remove and prevent the formation of

330 cell doublets. Importantly, due to the versatile nature of our acoustic forces, our technique does  
331 not require a cell-labeling step, and allows for the microfluidic channels and acoustic switching  
332 functionality to be integrated into a single device layer, which improves manufacturability,  
333 allows for the facile exchange of fluids, provides a good substrate for optical imaging, and has  
334 high chemical compatibility for patterning different biomolecules, which can be used for  
335 incubating cells and probing their molecular processes in future studies.

336

## 337 **Materials and Methods**

### 338 *Device Fabrication*

339 Three acoustofluidic arrays were tested in this study. Two had topside access ports in  
340 which holes were drilled through the glass prior to bonding. The other was fabricated by  
341 through-wafer etching of inlet/outlet ports and then bonding to unpatterned glass to enable  
342 backside fluidic access ports.<sup>56</sup> Photopatterning was achieved by spin coating Shipley S1838  
343 photoresist (MicroChemicals, GmbH) onto 6" silicon wafer (University Wafer, Inc.) at a spin  
344 speed of 3000 rpm, baking them at 115°C for 60 seconds, then exposing them to 126 mJ of 365  
345 nm UV radiation with a mask aligner (MA6/BA6, Karl Süss). These patterns served as a polymer  
346 mask for etching the microfluidic channels to a depth of approximately 18 µm using deep  
347 reactive ion etching (Pegasus deep silicon etcher; SPTS Technologies, Ltd.). We diced individual  
348 chips from the wafer when using the devices with topside access ports. For backside access  
349 ports, we used a second lithography step, in which the dice lines and inlets/outlet ports were  
350 patterned on the backside of the wafer in AZ9260 photoresist (MicroChemicals, GmbH), which  
351 was spin coated at 1800 rpm for 60 s, baked at 110°C for 3 min, then exposed to 3600 mJ of  
352 irradiation in the mask aligner. Subsequently, the wafer was bonded to a carrier and a through-  
353 silicon etch was performed using deep reactive ion etching. For both configurations, individual  
354 chips were cleaned in piranha and anodically bonded to precut glass cover slips (Borofloat®  
355 Glass; Schott AG) to form a hermetic seal (see Electronic Supplementary Information for  
356 Fabrication Routine for the Acoustofluidic Chip).

357

### 358 *Device Assembly*

359 The acoustofluidic chip was housed in a three-part aluminum manifold. The top  
360 component of the manifold uses standard ¼-28 threaded fittings (Idex Corp.) to make high

361 pressure (i.e. > 100 bar) world-to-chip connection to the acoustofluidic device with pressure tight  
362 fittings. The middle manifold had a recess along the top to hold the chip and another along the  
363 bottom to mount the zirconate titanate (PZT) transducers (1 1/8" x 1 1/16", resonant frequency,  
364  $f_0 = 1.35$  MHz; APC International, Ltd.), which were bonded to the manifold with cyanoacrylate  
365 glue (Loctite® 495; Loctite Corp.). We improved the acoustic transmission into the chip by  
366 spreading a layer of electrode gel (Spectra® 360; Parker Laboratories, Inc.) between the chip and  
367 manifold. Finally, the bottom component encloses the transducer in the manifold to enable a  
368 closed chamber for a temperature probe. For the backside configuration, access ports were  
369 included in the middle component (see Electronic Supplementary Information for Acoustofluidic  
370 Assembly with Backside Access Ports).

371

### 372 *Cell Preparation*

373 The PC9 cell line was cultured in RPMI 1640 with 10 % fetal bovine serum (FBS) and  
374 1% penicillin/streptomycin and maintained at 37°C in 5 % CO<sub>2</sub>. All cell lines were purchased  
375 from the Duke University Cell Culture Facility (CCF).

376

### 377 *Device Loading*

378 For microparticle studies, the chip was primed by sequentially rising with 190 proof  
379 ethanol (Sigma-Aldrich Corp.) and deionized water. After the chip was primed, 8.5 μm  
380 polystyrene beads (50,000 beads/ mL, Sigma Aldrich Corp.) suspended in 0.5 wt. %  
381 hexadecyltrimethylammonium bromide (CTAB) in deionized water were injected into the  
382 device. For cell studies, the chip was primed by sequentially rising with 190 proof ethanol  
383 (Sigma-Aldrich Corp.), 1X PBS buffer, and cell media (see cell preparation above). PC9 cells  
384 (400cells/ μL) were mixed with a biocompatible surfactant (Pluronic® F-68; Life Technologies,  
385 0.1 % v/v) and loaded into weirs under an oscillatory pressure profile (i.e. switching between  
386 pulses of -20 mbar for 8 seconds and 60 mbar for 2 seconds) from a reservoir at the outlet of the  
387 microfluidic chip using a pressure-controlled system (OB1 Pressure Controller; Elveflow). The  
388 oscillatory pressure profile was used to prevent cell adhesion or the formation of cell clusters on  
389 the back-side of weirs. After loading in the weirs, cells were transported to compartment sites  
390 using a three-step process. First, cells were withdrawn from weirs with negative pressure driven  
391 flow (i.e. -30 mbar) for 3 seconds then subsequently propelled towards the compartment region

392 at various pressures for 10 seconds. Next, when the particle reached the corner, the acoustic  
393 generator was switched ON, exciting the attached piezoelectric transducer with an acoustic  
394 sweep from 1.35 to 1.42 MHz with a sweep rate of 1 Hz and at over one second at an excitation  
395 of 16 V<sub>pp</sub>. Finally, after visually confirming that the particles in each field of view were captured  
396 at the corner, acoustics were turned off and cells were transported into compartment regions with  
397 positive pressure driven flow. We applied a positive pressure of ~30 mbar for relatively long  
398 durations of ~10 seconds, because this section had higher fluidic resistance and thus lower flow  
399 rates. Since there is a net positive pressure bias for each transfer cycle, cells that move into the  
400 compartments remain trapped there permanently. Meanwhile, it was possible to repeat this  
401 approach for cells that were missed during a previous cycle and still trapped in the weirs. After  
402 repeating this process 4-5 times, we were able to transfer a large percentage of the cells that were  
403 trapped in the first step.

404

#### 405 *Data Acquisition*

406 Switching efficiencies were determined by visually inspecting the particle trajectories  
407 when the acoustic field was turned on. Particle tracking data was extracted using a custom  
408 MATLAB program, which cropped a region of interest, stabilized the video, and extracted  
409 particle positions with circle tracking and thresholding. To quantify the frequency dependence of  
410 the trapping process, we used acoustic excitations at varying voltages and frequencies, and  
411 visually inspected the number of particles in the field of view (n=6) that were captured on the  
412 corners. An efficiency map was generated using a custom MATLAB script, with dark red circles  
413 indicating 100 % capture and blue circles indicating 0 % capture.

414 Additionally, to quantify the arraying efficiency across the chip acoustofluidic chips, we  
415 developed a custom Metamorph program (Molecular Devices, Inc.), which controlled the DMI-  
416 6000B microscope, XY automated stage (MS-2000; Applied Scientific Instrumentation) and  
417 camera to enable high-throughput imaging of each compartment in the array. Briefly, we first  
418 calculated the focal plane along the chip surface using fiducial alignment marks, and next bright  
419 field and fluorescent images were acquired in series along a prescribed XY path to map the entire  
420 array. The files were saved using a custom naming format, and then manually inspected to  
421 quantify the occupancy in the trap and compartment regions of the acoustofluidic element. Heat  
422 maps were created by recording the number of cells in each compartment in a table using a

423 custom MATLAB script to generate a color-coded grid indicating the occupancy of each  
424 compartment, with blue representing no cells and deep red representing three or more cells.

425

## 426 **Acknowledgements**

427 We would like to thank Elijah Weinreb for assistance in developing the Metamorph script  
428 and 3D printing the aluminum housings. This work was supported by an NSF graduate research  
429 fellowship (1106401) to K.A.O, a National Institutes of Health grants (R21GM111584,  
430 R21CA220082, and R01GM1234542), NSF's Research Triangle Materials Research Science and  
431 Engineering Center (DMR- 1121107), the Duke-Coulter Translational Partnership Grant  
432 Program, and was performed in part at the Duke University Shared Materials Instrumentation  
433 Facility (SMIF), a member of the North Carolina Research Triangle Nanotechnology Network  
434 (RTNN), which is supported by the National Science Foundation (Grant ECCS-1542015) as part  
435 of the National Nanotechnology Coordinated Infrastructure (NNCI).

436

437

## 438 **Author Contributions**

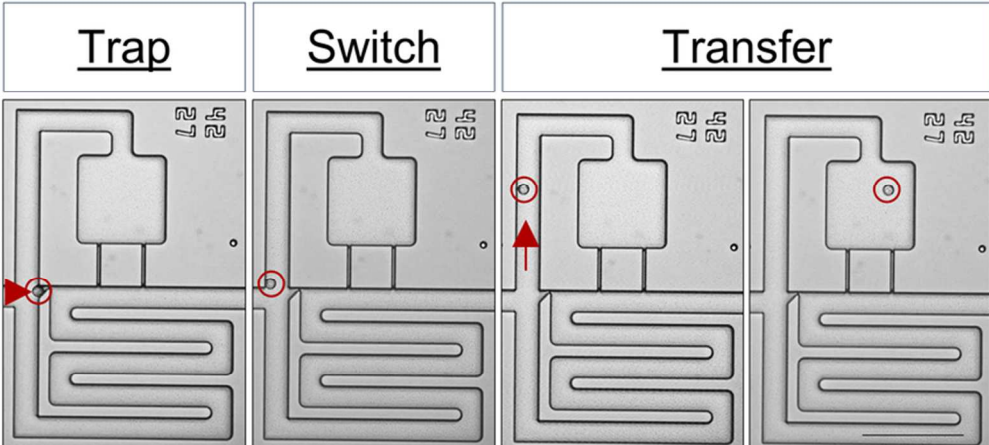
439 K.A.O. assisted in the design of the microfluidic chips, fabricated the devices, performed  
440 experiments, and prepared the manuscript. S.T.K. performed experiments and assisted in  
441 manuscript preparation. J.D.M. performed experiments and provided useful discussions for  
442 manuscript preparation. K.H.L. and K.C.W. provided cells for the experiments and useful  
443 discussions for manuscript preparation. B.B.Y. assisted in the design of the microfluidic chips  
444 and manuscript preparation.

445

446 **References**

- 447 1. M. B. Elowitz, A. J. Levine, E. D. Siggia and P. S. Swain, *Science*, 2002, **297**, 1183-1186.
- 448 2. A. K. Shalek, R. Satija, J. Shuga, J. J. Trombetta, D. Gennert, D. Lu, P. Chen, R. S. Gertner, J. T.  
449 Gaublomme, N. Yosef, S. Schwartz, B. Fowler, S. Weaver, J. Wang, X. Wang, R. Ding, R.  
450 Raychowdhury, N. Friedman, N. Hacohen, H. Park, A. P. May and A. Regev, *Nature*, 2014, **510**,  
451 363-369.
- 452 3. T. Kalisky and S. R. Quake, *Nat Methods*, 2011, **8**, 311-314.
- 453 4. A. K. Shalek and M. Benson, *Sci Transl Med*, 2017, **9**.
- 454 5. C. A. Vallejos, D. Risso, A. Scialdone, S. Dudoit and J. C. Marioni, *Nature Methods*, 2017, **14**,  
455 565-571.
- 456 6. S. Husic, S. K. Murthy and A. N. Koppes, *Anal Chem*, 2016, **88**, 354-380.
- 457 7. A. Gross, J. Schoendube, S. Zimmermann, M. Steeb, R. Zengerle and P. Koltay, *Int J Mol Sci*,  
458 2015, **16**, 16897-16919.
- 459 8. S. Tay, J. J. Hughey, T. K. Lee, T. Lipniacki, S. R. Quake and M. W. Covert, *Nature*, 2010, **466**,  
460 267-271.
- 461 9. C. Gawad, W. Koh and S. R. Quake, *Nat Rev Genet*, 2016, **17**, 175-188.
- 462 10. X. Zhang, S. L. Marjani, Z. Hu, S. M. Weissman, X. Pan and S. Wu, *Cancer Res*, 2016, **76**, 1305-  
463 1312.
- 464 11. A. Saadatpour, S. J. Lai, G. J. Guo and G. C. Yuan, *Trends Genet*, 2015, **31**, 576-586.
- 465 12. D. J. Wang and S. Bodovitz, *Trends Biotechnol*, 2010, **28**, 281-290.
- 466 13. P. Hu, W. Zhang, H. Xin and G. Deng, *Front Cell Dev Biol*, 2016, **4**, 116.
- 467 14. A. M. Thompson, A. L. Paguirigan, J. E. Kreutz, J. P. Radich and D. T. Chiu, *Lab Chip*, 2014,  
468 **14**, 3135-3142.
- 469 15. J. C. Love, *Aiche J*, 2010, **56**, 2496-2502.
- 470 16. S. Yamamura, H. Kishi, Y. Tokimitsu, S. Kondo, R. Honda, S. R. Rao, M. Omori, E. Tamiya and  
471 A. Muraguchi, *Analytical Chemistry*, 2005, **77**, 8050-8056.
- 472 17. T. M. Gierahn, M. H. Wadsworth, 2nd, T. K. Hughes, B. D. Bryson, A. Butler, R. Satija, S.  
473 Fortune, J. C. Love and A. K. Shalek, *Nat Methods*, 2017, **14**, 395-398.
- 474 18. W. H. Tan and S. Takeuchi, *P Natl Acad Sci USA*, 2007, **104**, 1146-1151.
- 475 19. D. Di Carlo, L. Y. Wu and L. P. Lee, *Lab on a Chip*, 2006, **6**, 1445-1449.
- 476 20. T. Teshima, H. Ishihara, K. Iwai, A. Adachi and S. Takeuchi, *Lab on a Chip*, 2010, **10**, 2443-  
477 2448.
- 478 21. R. J. Kimmerling, G. Lee Szeto, J. W. Li, A. S. Genshaft, S. W. Kazer, K. R. Payer, J. de Riba  
479 Borrajo, P. C. Blainey, D. J. Irvine, A. K. Shalek and S. R. Manalis, *Nat Commun*, 2016, **7**,  
480 10220.
- 481 22. L. Mi, L. Huang, J. X. Li, G. Q. Xu, Q. Wu and W. H. Wang, *Lab on a Chip*, 2016, **16**, 4507-  
482 4511.
- 483 23. W. Liu, N. Dechev, I. G. Foulds, R. Burke, A. Parameswaran and E. J. Park, *Lab on a Chip*,  
484 2009, **9**, 2381-2390.
- 485 24. A. Chen, T. Byvank, W. J. Chang, A. Bharde, G. Vieira, B. L. Miller, J. J. Chalmers, R. Bashir  
486 and R. Sooryakumar, *Lab on a Chip*, 2013, **13**, 1172-1181.
- 487 25. L. Mazutis, J. Gilbert, W. L. Ung, D. A. Weitz, A. D. Griffiths and J. A. Heyman, *Nat Protoc*,  
488 2013, **8**, 870-891.
- 489 26. F. Guo, Z. M. Mao, Y. C. Chen, Z. W. Xie, J. P. Lata, P. Li, L. Q. Ren, J. Y. Liu, J. Yang, M.  
490 Dao, S. Suresh and T. J. Huang, *P Natl Acad Sci USA*, 2016, **113**, 1522-1527.
- 491 27. K. R. Love, S. Bagh, J. Choi and J. C. Love, *Trends Biotechnol*, 2013, **31**, 16-22.
- 492 28. A. J. Torres, A. S. Hill and J. C. Love, *Anal Chem*, 2014, **86**, 11562-11569.
- 493 29. L. D. Goldstein, Y. J. Chen, J. Dunne, A. Mir, H. Hubschle, J. Guillory, W. Yuan, J. Zhang, J.  
494 Stinson, B. Jaiswal, K. B. Pahuja, I. Mann, T. Schaal, L. Chan, S. Anandakrishnan, C. W. Lin, P.

- 495 Espinoza, S. Husain, H. Shapiro, K. Swaminathan, S. Wei, M. Srinivasan, S. Seshagiri and Z.  
496 Modrusan, *BMC Genomics*, 2017, **18**, 519.
- 497 30. Y. H. Cheng, Y. C. Chen, R. Brien and E. Yoon, *Lab Chip*, 2016, **16**, 3708-3717.
- 498 31. C. H. Lin, Y. H. Hsiao, H. C. Chang, C. F. Yeh, C. K. He, E. M. Salm, C. Chen, I. M. Chiu and  
499 C. H. Hsu, *Lab Chip*, 2015, **15**, 2928-2938.
- 500 32. Y. Li, J. H. Jang, C. Wang, B. He, K. Zhang, P. Zhang, T. Vu and L. Qin, *Advanced Biosystems*,  
501 2017, **1**.
- 502 33. R. Abedini-Nassab, D. Y. Joh, F. Albarghouthi, A. Chilkoti, D. M. Murdoch and B. B. Yellen,  
503 *Lab on a Chip*, 2016, **16**, 4181-4188.
- 504 34. R. Abedini-Nassab, D. Y. Joh, M. A. Triggiano, C. Baker, A. Chilkoti, D. M. Murdoch and B. B.  
505 Yellen, *Adv Funct Mater*, 2016, **26**, 4026-4034.
- 506 35. P. Y. Chiou, A. T. Ohta and M. C. Wu, *Nature*, 2005, **436**, 370-372.
- 507 36. P. Y. Chiou, W. Wong, J. C. Liao and M. C. Wu, *Proc Ieee Micr Elect*, 2004, 21-24.
- 508 37. M. C. Wu, *Nat Photonics*, 2011, **5**, 322-324.
- 509 38. H. Y. Hsu, A. Jamshidi, S. Shekarchian, W. Lam, J. K. Valley, S. N. Pei and M. C. Wu, *2011*  
510 *Ieee 24th International Conference on Micro Electro Mechanical Systems (Mems)*, 2011, 63-66.
- 511 39. D. J. Collins, B. Morahan, J. Garcia-Bustos, C. Doerig, M. Plebanski and A. Neild, *Nat Commun*,  
512 2015, **6**, 8686.
- 513 40. B. Vanherberghen, O. Manneberg, A. Christakou, T. Frisk, M. Ohlin, H. M. Hertz, B. Onfelt and  
514 M. Wiklund, *Lab on a Chip*, 2010, **10**, 2727-2732.
- 515 41. H. Bruus, *Lab on a Chip*, 2012, **12**, 1014-1021.
- 516 42. J. D. Adams, P. Thevoz, H. Bruus and H. T. Soh, *Appl Phys Lett*, 2009, **95**, 254103.
- 517 43. S. M. Hagsater, T. G. Jensen, H. Bruus and J. P. Kutter, *Lab Chip*, 2007, **7**, 1336-1344.
- 518 44. K. A. Ohiri, B. A. Evans, C. W. Shields, R. A. Gutierrez, N. J. Carroll, B. B. Yellen and G. P.  
519 Lopez, *Acs Applied Materials & Interfaces*, 2016, **8**, 25030-25035.
- 520 45. C. W. Shields Iv, J. L. Wang, K. A. Ohiri, E. D. Essoyan, B. B. Yellen, A. J. Armstrong and G. P.  
521 Lopez, *Lab Chip*, 2016, **16**, 3833-3844.
- 522 46. D. Ahmed, A. Ozcelik, N. Bojanala, N. Nama, A. Upadhyay, Y. C. Chen, W. Hanna-Rose and T.  
523 J. Huang, *Nature Communications*, 2016, **7**.
- 524 47. X. Ding, P. Li, S. C. Lin, Z. S. Stratton, N. Nama, F. Guo, D. Slotcavage, X. Mao, J. Shi, F.  
525 Costanzo and T. J. Huang, *Lab Chip*, 2013, **13**, 3626-3649.
- 526 48. M. Kaynak, A. Ozcelik, A. Nourhani, P. E. Lammert, V. H. Crespi and T. J. Huang, *Lab Chip*,  
527 2017, **17**, 395-400.
- 528 49. L. Y. Yeo and J. R. Friend, *Annu Rev Fluid Mech*, 2014, **46**, 379-406.
- 529 50. Y. H. Hsu, M. L. Moya, P. Abiri, C. C. Hughes, S. C. George and A. P. Lee, *Lab Chip*, 2013, **13**,  
530 81-89.
- 531 51. I. Leibacher, P. Hahn and J. Dual, *Microfluid Nanofluid*, 2015, **19**, 923-933.
- 532 52. V. H. Lieu, T. A. House and D. T. Schwartz, *Analytical chemistry*, 2012, **84**, 1963-1968.
- 533 53. A. Karimi, S. Yazdi and A. M. Ardekani, *Biomicrofluidics*, 2013, **7**.
- 534 54. A. Ozcelik, D. Ahmed, Y. Xie, N. Nama, Z. Qu, A. A. Nawaz and T. J. Huang, *Anal Chem*, 2014,  
535 **86**, 5083-5088.
- 536 55. M. Ovchinnikov, J. Zhou and S. Yalamanchili, *J Acoust Soc Am*, 2014, **136**, 22-29.
- 537 56. C. W. Shields, D. F. Cruz, K. A. Ohiri, B. B. Yellen and G. P. Lopez, *Jove-Journal of Visualized*  
538 *Experiments*, 2016, DOI: 10.3791/53861.



36x17mm (600 x 600 DPI)